Paleoceanography and Paleoclimatology

RESEARCH ARTICLE
10.1029/2022PA004530

# Hydroclimate Variability in the Equatorial Western Indian Ocean for the Last 250,000 Years

**Grace Windler[1], Jessica E. Tierney[1], and Peter B. deMenocal[2]**

[1]Department of Geosciences, University of Arizona, Tucson, AZ, USA, [2]Lamont-Doherty Earth Observatory, Columbia University, Palisades, NY, USA

**Key Points:**

- New multi-proxy reconstructions from the tropical western Indian Ocean show both precession and glacial-interglacial variability
- A new precipitation isotope record likely reflects large-scale Indian summer monsoon circulation changes over time
- Glacial-scale changes in upper water column structure across the Indian Ocean support shelf exposure as a primary hydroclimate influence

**Supporting Information:**

Supporting Information may be found in the online version of this article.

**Correspondence to:**

G. Windler,
gwindler@arizona.edu

**Citation:**

Windler, G., Tierney, J. E., & deMenocal, P. B. (2023). Hydroclimate variability in the equatorial western Indian Ocean for the last 250,000 years. *Paleoceanography and Paleoclimatology*, *38*, e2022PA004530. https://doi.org/10.1029/2022PA004530

Received 14 AUG 2022
Accepted 18 JAN 2023



**Abstract** Indian Ocean sea surface temperatures impact precipitation across the basin through coupled ocean-atmosphere responses to changes in climate. To understand the hydroclimate response over the western Indian Ocean and equatorial east Africa to different forcing mechanisms, we present four new proxy reconstructions from core VM19-193 (2.98°N, 51.47°E) that span the last 250 ky. Sub-surface water temperatures (Sub-T; $TEX_{86}$) show strong precessional (23 ky) variability that is primarily influenced by maximum incoming solar radiation (insolation) during the Northern Hemisphere spring season, likely indicating that local insolation dominates the upper water column at this tropical location over time. Leaf waxes, on the other hand, reflect two different precipitation signals: $\delta^{13}C_{wax}$ (in phase with boreal fall insolation) is likely reflecting vegetation changes in response to local rainfall over east Africa, whereas $\delta D_{precip}$ (primarily driven by boreal summer insolation) represents changes in regional circulation associated with the summer monsoon. Glacial-interglacial changes in ocean temperatures support glacial shelf exposure over the Maritime Continent in the eastern Indian Ocean and the subsequent weakening of the Indian Walker Circulation as a mechanism driving 100 ky climate variability across the tropical Indo-Pacific. Additionally, the 100 ky spectral power in $\delta D_{precip}$ supports a basin-wide weakening of summer monsoon circulation in response to glacial climates. Overall, the proxy records from VM19-193 indicate that both precession and glacial-interglacial cycles exert control over hydroclimate at this tropical location.

## 1. Introduction

Sea surface temperatures (SSTs) across the Indian Ocean (IO) basin have a strong influence on precipitation patterns over nearby regions via coupled ocean-atmosphere feedbacks (Saji et al., 1999; Tierney et al., 2013; Tokinaga et al., 2012). The entire IO has been warming since at least the mid-20th century (Alory et al., 2007) with the western tropical IO warming at a much faster rate, even relative to the rest of the tropics (W. Cai et al., 2014; Roxy et al., 2014). Changes in the tropical IO SST gradient are expected to increase the frequency and intensity of climate modes such as the IO dipole (W. Cai et al., 2014; DiNezio et al., 2020). During positive dipole events, the SST gradient weakens the Walker Circulation over the IO and increases convective activity over the western IO leading to increased precipitation over equatorial east Africa and the potential for drought over Sumatra (Saji et al., 1999). Another major climate feature of the IO basin is the Indian summer monsoon, driven by intense heating of the land surface over northern India during Northern Hemisphere (NH) summer leading to strong land-sea temperature contrasts and pressure gradients (Molnar et al., 2010). The pressure gradients drive cross-equatorial winds that pick up speed and curve toward the northeast off the east African coast via the Somali Jet (Schott & McCreary, 2001; Schott et al., 2009). Past climate changes can help shed light on the IO SST gradient and Indian summer monsoon response to external drivers.

Pleistocene climate reconstructions are characterized by rhythmic climate changes that correspond with 23- (precession), 41- (obliquity/tilt), and 100-ky (eccentricity/glacial-interglacial) cycles (Laskar et al., 2004; Ruddiman, 2006). The cyclic configurations of Earth's orbit control the seasonal and latitudinal distribution of incoming solar radiation (insolation). Precession, which controls the seasonal amount of insolation, is thought to be the dominant control on tropical climate during the Pleistocene (Clement et al., 2004; Jalihal et al., 2019; Merlis et al., 2013); however, reconstructions long enough to span multiple glacial cycles from the Indo-Pacific Warm Pool exhibit clear 100 ky glacial-interglacial variability (Lea, 2004; Lückge et al., 2009; Windler et al., 2019b, 2021). Exposure of the Sunda and Sahul Shelves in the Warm Pool during glacial periods is thought to trigger a dipole-like response across the tropical IO (DiNezio & Tierney, 2013; DiNezio et al., 2016, 2018), suggesting that glacial-interglacial variability should be important in the western IO as it is in the eastern IO.

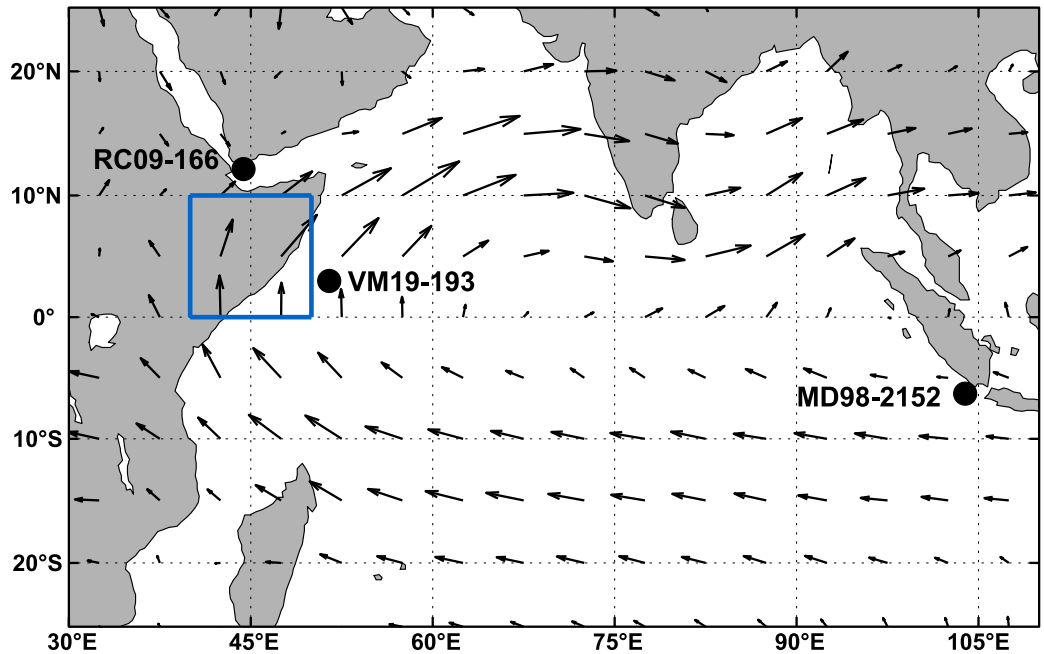


**Figure 1.** Map of the core sites discussed in this text. Vectors represent the average 850 mb winds from June–September, from the NCEP/NCAR Reanalysis product (Kanamitsu et al., 2002). Blue rectangle denotes area averaged for annual precipitation in Figure 2b.

Paleoclimate reconstructions from the Arabian Sea vary predominantly with precession and are thought to reflect the intensity of the summer monsoon (S. Clemens & Prell, 2003; S. Clemens et al., 1991), whereas records from the Gulf of Aden and the Omani coast show a mixed influence of precession and glacial-interglacial cycles on overall climate variability (Anderson & Prell, 1993; Tierney et al., 2017a). Currently, there is a lack of multi-proxy climate reconstructions spanning multiple glacial cycles from the western IO outside of the Arabian Sea upwelling zone, meaning there is a sparsity of reconstruction data from the equatorial western IO to examine cross-basin hydroclimate responses over time.

Here we present four new proxy reconstructions from the western IO, outside of the primary Indian summer monsoon domain, that span approximately 250 ky. Specifically, we examine SSTs using the $U^{K'}_{37}$ index, sub-surface temperatures (Sub-Ts) using the $TEX_{86}$ index, and the isotopic composition of regional precipitation and vegetation using terrestrial leaf waxes ($\delta$D and $\delta^{13}$C). We use singular spectrum analysis (SSA) to isolate the leading signals, or modes of variability, in the data. We then use cross-spectral analysis to examine the coherency and phase of these leading modes in the proxy reconstructions with maximum NH summer insolation to determine the major influences on precipitation, circulation, and upper ocean temperatures in the tropical western IO for the last 250 ky.

### 1.1. Modern Climatology of VM19-193

Marine core VM19-193 (2.98°N, 51.47°E) was obtained in August 1963 as part of the Vema cruise VM19 from a water depth of 5,106 m in the western IO (Figure 1). VM19-193 is 10.78 m long and consists of alternating carbonate-rich and carbonate-poor sediment layers, which mark glacial to interglacial transitions and were used in our age model construction (Figure 3). The likely source of terrestrial material to this site is equatorial east Africa and the Horn of Africa, east of the topographic highlands of Ethiopia and Kenya. Vegetation in the equatorial lowlands near the coast in this region largely consists of a grass savannah (Schefuβ et al., 2003). Precipitation peaks during two seasons in this area: a primary peak during the "long rains" in April and May when the Intertropical Convergence Zone passes overhead as it shifts northward and a secondary peak during the "short rains" in October and November as it shifts back southward (Figure 2b). The major moisture source to this area is the nearby IO.

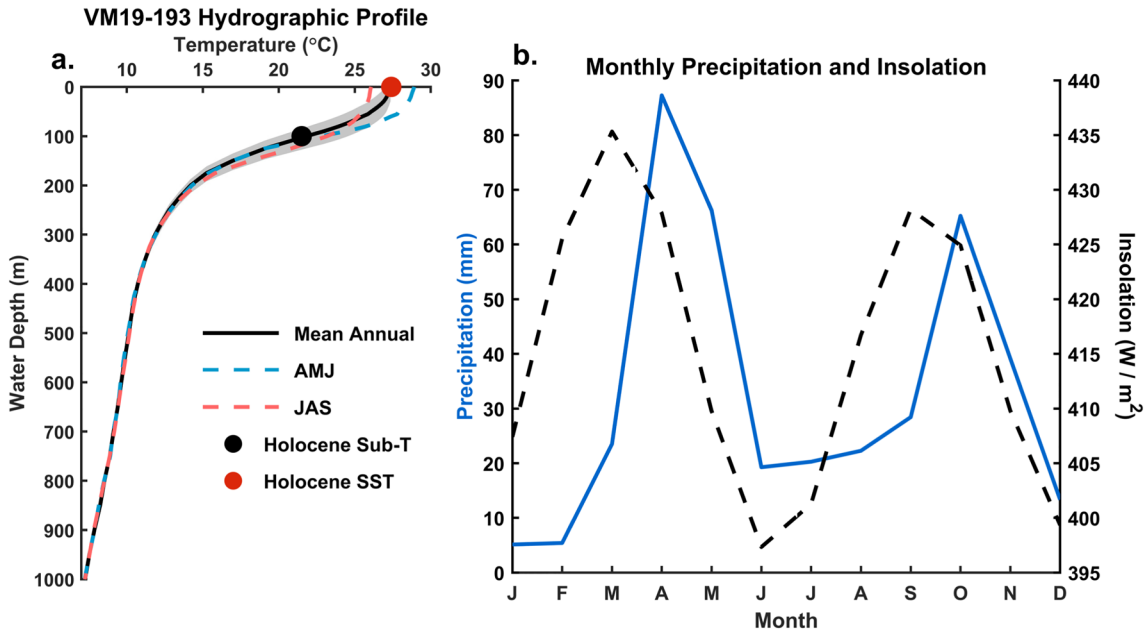


**Figure 2.** (a) Water temperature versus depth at VM19-193. Data plotted from the World Ocean Atlas 2018 1° resolution data set for the period 1955–2017 (Locarnini et al., 2018). Mean annual, NH spring (AMJ), and NH summer (JAS) temperatures are plotted. Gray shading indicates 1$\sigma$ around mean annual temperatures. (b) Monthly GPCC Precipitation data (1° resolution from 1891 to 2016) averaged over 0–10°N and 40–50°E (see blue rectangle in Figure 1) (Schneider et al., 2011, 2016). Dashed line represents monthly local insolation at VM19-193 (CERES Edition 4.0 data product from 2000–present) (Loeb et al., 2018). GPCC Precipitation data provided by the NOAA/OAR/ESRL PSL from their website. Points in panel a show calculated mean annual Holocene sea surface temperature and Sub-T from the $U^{K'}_{37}$ and $TEX_{86}$ proxies, respectively, measured in the uppermost section of VM19-193.

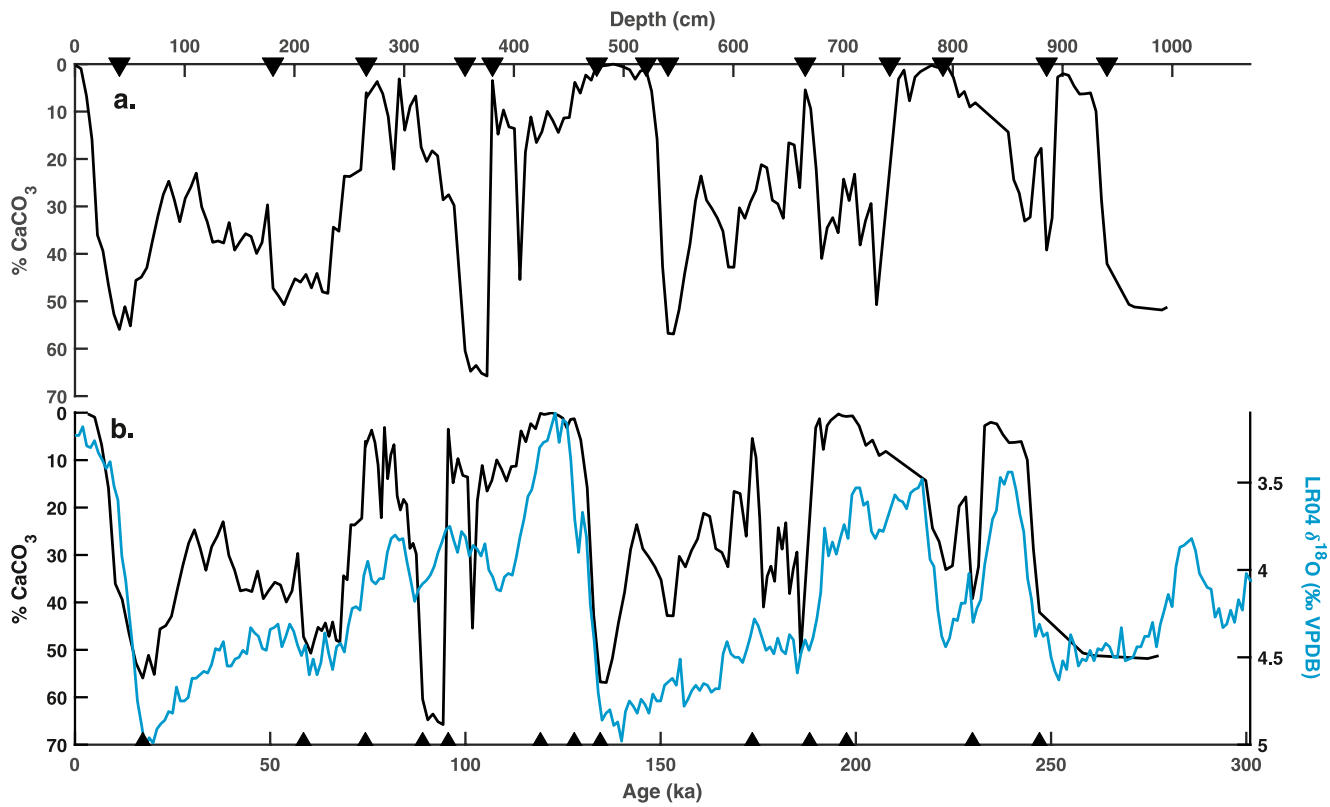


**Figure 3.** VM19-193 %$CaCO_3$ plotted (a) versus depth and (b) versus age with the benthic $\delta^{18}O$ stack (Lisiecki & Raymo, 2005). Tie points for the age model are denoted as black triangles in both depth and age space.

SSTs at VM19-193 are fairly warm year-round (>26°C), but exhibit small seasonal changes: the warmest SSTs occur in the spring corresponding to a peak in local insolation, whereas the coldest SSTs occur in the summer (Figure 2a). Not only is VM19-193 in the pathway of the Somali Jet, but it is also located just south of a seasonal upwelling wedge off the Somali coast (Schott et al., 2009); therefore, the slightly colder summer SSTs here reflect both increased surface evaporation from strengthened monsoon winds and cooler water that upwells off the Somali coast and gets diverted southward (back toward the equator) (Schott et al., 2009). Conversely, the thermocline does not change much seasonally (Figure 2a).

### 1.2. Paleoclimate Proxies

Alkenones are long-chain ($C_{37}$) ketones produced by *Emiliania huxleyi*, a marine phytoplankton that lives throughout Earth's surface oceans (Prahl & Wakeham, 1987; Volkman et al., 1980). The number of unsaturations in the alkenone structure varies with the temperature of the water in which the organism grows, thus reflecting SSTs (Brassell et al., 1986). The alkenone unsaturation index reflects the ratio of di- and tri-unsaturated alkenones in a given sample as follows: $U^{K'}_{37} = [C_{37:2}]/([C_{37:2}] + [C_{37:3}])$, where $U^{K'}_{37}$ values approaching 1 reflect warmer temperatures (Prahl & Wakeham, 1987). One potential issue with $U^{K'}_{37}$ in warm tropical regions, such as our study site, is the non-linear sensitivity of alkenones to high temperatures (>24°C) (Conte et al., 2006; T. I. Eglinton & Eglinton, 2008). The BAYSPLINE calibration for converting $U^{K'}_{37}$ values to SSTs addresses this issue with a non-linear Bayesian regression model (Tierney & Tingley, 2018). Seasonal biases in the production of alkenones could also skew the temperature estimates away from mean annual values, but this is largely a problem at high latitudes (Conte et al., 2006; Tierney & Tingley, 2018). Seasonal SST variability at VM19-193 is small and mean Holocene SST values reconstructed from VM19-193 are consistent with modern mean annual surface temperatures (Figure 2a), so alkenones here likely capture mean annual temperatures.

Isoprenoidal glycerol dialkyl glycerol tetraethers (GDGTs) are membrane lipids produced by marine archaea and contain a different number of pentacyclic rings, depending on water temperature (Schouten et al., 2002). $TEX_{86}$ (TetraEther indeX of 86 carbons) describes the relative amount of cyclization of GDGTs in which values closer to 1 reflect a greater number of rings and higher water temperatures (Schouten et al., 2007; Wuchter et al., 2004): $TEX_{86} = ([GDGT\text{-}2] + [GDGT\text{-}3] + [cren'])/([GDGT\text{-}1] + [GDGT\text{-}2] + [GDGT\text{-}3] + [cren'])$, where cren′ refers to the isomer of crenarchaeol, a characteristic lipid of Thaumarchaeota, the primary producers of isoprenoidal GDGTs. While $TEX_{86}$ values are empirically related to SSTs (Schouten et al., 2002), Thaumarchaeota can live throughout the water column with greatest abundances from 0 to 200 m (Church et al., 2010), thus $TEX_{86}$ can also reflect subsurface temperatures (Sub-T) (Chen et al., 2016; Lopes dos Santos et al., 2010). At Site VM19-193, conversion of the Holocene $TEX_{86}$ values using the BAYSPAR SST calibration yields temperatures (ca. 24.5°C) that are substantially colder than mean annual SST (ca. 26°C) and also cooler than the alkenone-inferred SSTs (Figure 2a). In addition, the GDGT-2/GDGT-3 ratio of the Holocene samples is 7.2, which at a $TEX_{86}$ value of 0.670 lies to the right of the pure temperature-dependent relationship between these indices established by Rattanasriampaipong et al. (2022), indicating some deeper water input to the sedimentary GDGTs (although not an extreme amount). Therefore, we chose to interpret our $TEX_{86}$ data to indicate Sub-T variability. We calibrate our data with the BAYSPAR Sub-T calibration, which predicts gamma-weighted integrated temperatures for 0–200 m water depths from $TEX_{86}$ values with a peak probability at 50 m (Tierney & Tingley, 2015). Mean Holocene Sub-Ts reconstructed from VM19-193 are consistent with modern temperatures at the thermocline, suggesting that this calibration and the Sub-T interpretation is appropriate (Figure 2a). In addition, thermocline steepness at VM19-193 exhibits little-to-no seasonal difference (Figure 2a), thus we interpret $TEX_{86}$ to indicate mean annual Sub-T.

The wax layer of terrestrial plant leaves is composed of long-chain (>$C_{25}$) *n*-alkanes and *n*-alkanoic acids, also known as fatty acids (G. Eglinton & Hamilton, 1967), which are geologically stable and accumulate in sediment via runoff and wind (T. I. Eglinton & Eglinton, 2008). Terrestrial leaf wax $\delta D$ ($\delta D_{wax}$) reflects the $\delta D$ of the plant's source water; therefore, waxes extracted from sediments, which are contributed by regional vegetation, reflect the $\delta D$ variability of regional precipitation ($\delta D_{precip}$) over time. The apparent offset between $\delta D_{wax}$ and $\delta D_{precip}$ ($\varepsilon_{water-wax}$) varies between different plant types and photosynthetic pathways, where monocots (grasses) exhibit a larger $\varepsilon_{water-wax}$ during leaf wax synthesis than other vascular plants (Gao et al., 2014; Sachse et al., 2012). Photosynthetic pathways among grasses also affect $\varepsilon_{water-wax}$: $C_3$ grasses synthesize waxes that are more depleted in D relative to precipitation than $C_4$ grasses, meaning that $C_4$ grasses exert a smaller $\varepsilon_{water-wax}$ than their $C_3$ counterparts

**Table 1**
*VM19-193 Age Model Information*

| Depth(cm) | Tie Point(ka) | OxCal Median(ka) | OxCal 1$\sigma$(ky) |
|---|---|---|---|
| 0 | – | 3.1 | ±1.4 |
| 40.5 | 18 | 17.4 | ±1.8 |
| 180.5 | 60 | 58.5 | ±1.8 |
| 265.5 | 75 | 74.4 | ±1.6 |
| 355.5 | 87 | 89.0 | ±1.6 |
| 380.5 | 96 | 95.6 | ±1.7 |
| 475.5 | 120 | 119.2 | ±1.7 |
| 520.5 | 126 | 127.9 | ±1.6 |
| 540.5 | 135 | 134.5 | ±1.7 |
| 665.5 | 175 | 173.5 | ±1.8 |
| 742.5 | 188 | 188.2 | ±1.6 |
| 791 | 196 | 197.6 | ±1.7 |
| 885.5 | 230 | 229.9 | ±1.8 |
| 940.5 | 246 | 247.0 | ±1.9 |

*Note*. Includes %$CaCO_3$ tie points, median modeled ages, and 1$\sigma$ uncertainty using OxCal version 4.4.

(Sachse et al., 2012). The carbon isotope composition of leaf waxes ($\delta^{13}C_{wax}$) also differs between $C_3$ (~−30‰ $\delta^{13}C_{wax}$) and $C_4$ (~−20‰ $\delta^{13}C_{wax}$) plants, reflecting the different degree of fractionation between each photosynthetic pathway (T. I. Eglinton & Eglinton, 2008; Sachse et al., 2012). The $\delta^{13}C_{wax}$ values extracted from sediments thus indicate changes in the relative contribution of $C_3$ versus $C_4$ plant types from regional vegetation through time. Here, we use the $\delta^{13}C_{wax}$ in tandem with $\delta D_{wax}$ measurements from VM19-193 to account for regional vegetation influence on $\varepsilon_{water-wax}$. The closest continental margin is the likely source of leaf waxes to VM19-193, that is, equatorial east Africa, including the sparsely vegetated Horn of Africa and southern Somalia and Kenya (Figure 1).

## 2. Materials and Methods

### 2.1. VM19-193 Age Model

Due to the depth of the site, preservation of foraminifera is poor in VM19-193, which precludes us from using either planktic or benthic foraminifera to construct an age model. Instead, the VM19-193 age model is based on tie points between bulk $CaCO_3$ measurements in the core and the global benthic foraminifera $\delta^{18}O$ stack from Lisiecki and Raymo (2005) (Figure 3, Table 1). This approach is rooted in the fact that the carbonate compensation depth, or CCD, in the deep western equatorial IO near the Somali Basin closely tracks glacial and interglacial periods during the Quaternary (Divakar Naidu et al., 1993). Specifically, the CCD was deeper during glacial periods relative to today, resulting in better $CaCO_3$ preservation during cooler periods. Bulk $CaCO_3$ was measured by coulometry at Lamont-Doherty Earth Observatory. Some glacial terminations are identifiable as sudden transitions to near 0% $CaCO_3$ (e.g., the termination of the Last Glacial Maximum, Figure 3). Other transitions are more gradual, so depth tie points were chosen based on shifts between carbonate-rich and carbonate-poor sediment in the core description and photographs. We used the P sequence routine in OxCal version 4.4 to generate the age model (Bronk Ramsey, 2008), the inputs and results of which are summarized in Table 1. We find no evidence of sudden sedimentation rate changes throughout the core, including near glacial-interglacial transitions (Figure S1 in Supporting Information S1). The overall sedimentation rate is approximately 3.6 cm/ky ±0.5 cm/ky 1$\sigma$. The %$CaCO_3$ record ends at the 995 cm depth (Figure 3a). The core description and pictures show a sharp contact and large irregular patch below approximately 940 cm; therefore, we do not present proxy data beyond that depth.

### 2.2. Organic Geochemical Analyses

A total of 107 samples from VM19-193—taken approximately every 10 cm and averaging 19 g of sediment per sample—94 of which were from depths of 940 cm and above, were freeze-dried before total lipid extraction, which was performed on a Thermo (DIONEX) accelerated solvent extractor with a 9:1 (*v*/*v*) mixture of dichloromethane:methanol. Internal standards were added to each lipid extract for compound quantification: 5,000 ng of a general recovery standard consisting of stearyl stearate (for alkenones) and cis-11-eicosanoic acid (for fatty acids) and 2,000 ng of a $C_{46}$ GDGT standard. The different compounds were separated using column chromatography with a layered 1:1 solid phase of LC-$NH_2$ (bottom layer) and 5% deactivated silica (top layer) gels. Separation of alkenones, GDGTs, and fatty acids was achieved using the solvents dichloromethane, dichloromethane:isopropanol (2:1), and 4% acetic acid in dichloromethane, respectively and in that order.

Alkenones were analyzed on an Agilent 7890 gas chromatograph (GC) with a programmable temperature vapourization inlet. The inlet and oven temperature programs were those described by Windler et al. (2019b). Approximately 20% of the alkenone samples were run in duplicate with an average analytical error of ±0.006 $U^{K'}_{37}$ units (±0.3°C). To convert $U^{K'}_{37}$ values to temperature, we used the BAYSPLINE calibration (Tierney & Tingley, 2018), which is non-linear at warm temperatures providing more realistic values as $U^{K'}_{37}$ values approach one.

Glycerol dialkyl glycerol tetraethers were filtered with a 99:1 mixture of hexane:isopropanol prior to analysis on an Agilent 6210 single quadropole mass spectrometer with a 1260/1290 high performance liquid chromatograph.

The liquid chromatograph method, modified from Hopmans et al. (2016), and the binary solvent pump timetable were those described in Windler et al. (2019b). Approximately 20% of the GDGT samples were run in duplicate with an average analytical error of ±0.003 $TEX_{86}$ units (±0.2°C). To convert $TEX_{86}$ values to temperature, we used the BAYSPAR Sub-T calibration (Tierney & Tingley, 2015), which predicts gamma-weighted integrated temperatures in the top 200 m of the water column.

Fatty acids were methylated over night using methanol with a known isotopic composition to form fatty acid methyl esters (FAMEs), then further purified using a final column chromatography step with silica gel as the solid phase. The $\delta^{13}C$ and $\delta D$ of FAMEs were analyzed separately using a Thermo Scientific Delta V Plus stable isotope mass spectrometer with a Conflo IV, Trace 1310 GC, and GC Isolink II. External FAME and *n*-alkane standards of known isotopic composition were run every five injections to monitor drift and ensure accuracy. Higher chain leaf wax fatty acids ($\geq C_{28}$) are largely produced by terrestrial vascular plants (Kusch et al., 2010), but aquatic sources with chain lengths as high as $C_{28}$ have been detected (Feakins et al., 2007; Volkman et al., 1980). To avoid the influence of aquatic material we measured $\delta^{13}C$ and $\delta D$ values of the $C_{30}$ fatty acid. All samples were run in at least duplicate for both carbon and hydrogen analyses. Approximately 25% were run in triplicate for $\delta D$ with an overall analytical precision of ±1.4‰ (1$\sigma$). Approximately 15% of the samples were run in triplicate for $\delta^{13}C$ with an overall precision of ±0.1‰ (1$\sigma$). All $\delta D$ values are reported in ‰ notation versus Vienna Standard Mean Ocean Water. All $\delta^{13}C$ values are reported in ‰ notation versus Vienna Pee Dee Belemnite (VPDB). Measurements were corrected for the carbon and hydrogen isotopes added during the methylation process using mass balance.

### 2.3. Vegetation Correction

As previously mentioned, the fractionation of leaf wax isotopes ($\varepsilon_{water-wax}$) varies between different plant types and photosynthetic pathways (Feakins & Sessions, 2010; Sachse et al., 2012; Smith & Freeman, 2006). To account for changes in $\varepsilon_{water-wax}$ over time, we use an established Bayesian method to infer $\delta D_{precip}$ from $\delta D_{wax}$ (Bhattacharya et al., 2018; Tierney et al., 2017; Windler et al., 2020). We use paired $\delta^{13}C_{wax}$ measurements from VM19-193 to estimate the fractional contribution of leaf waxes from $C_4$ plants ($f_{C4}$) in each sample, using designated $\delta^{13}C_{C3}$ and $\delta^{13}C_{C4}$ endmembers (Tierney et al., 2017). Estimated $f_{C4}$ and designated endmember values of $\varepsilon_{C3}$ and $\varepsilon_{C4}$ are used to calculate a vegetation-weighted $\varepsilon_{water-wax}$ for each sample (Equation 1). The $\varepsilon_{water-wax}$ values are then used to calculate $\delta D_{precip}$ (Equation 2):

$$\varepsilon_{water-wax} = f_{C4} \times \epsilon_{C4} + (1 - f_{C4}) \times \epsilon_{C3} \quad (1)$$

$$\delta D_{precip} = \frac{1,000 + \delta D_{wax}}{\left(\frac{\varepsilon_{water-wax}}{1,000}\right) + 1} - 1,000 \quad (2)$$

We use the following endmember values (±standard error) from the "All Africa" data set (Garcin et al., 2014): $\delta^{13}C_{C3} = -33.4 \pm 0.4$‰ and $\delta^{13}C_{C4} = -19.8 \pm 0.3$‰. For $\varepsilon_{water-wax}$ endmembers (±standard error), we use values from Sachse et al. (2012): $\varepsilon_{C3} = -114 \pm 2.1$‰ (excluding grasses) and $\varepsilon_{C4} = -132 \pm 3.3$‰ (monocots only). All endmember values correspond to $C_{29}$-alkane $\delta^{13}C$ and $\varepsilon_{water-wax}$, since comparable data do not exist for the $C_{30}$ fatty acid; however, fractionation between the two appear to be closely related (Gao et al., 2014), so we assume they are equivalent. The raw $\delta D_{wax}$, corrected $\delta D_{precip}$, and $f_{C4}$ values are shown in Figure S2 in Supporting Information S1.

### 2.4. Singular Spectrum and Cross Spectral Analyses

To isolate the leading oscillatory modes of variability in each reconstruction we perform a SSA on each record (Allen & Smith, 1996, 1997; Ghil et al., 2002). A "trajectory matrix" is constructed using $M$ lagged copies of a centered, evenly spaced time series, then the empirical orthogonal functions are calculated from the covariance matrix of the lagged series (Ghil et al., 2002; Ghil & Vautard, 1991; Vautard et al., 1992). We resample the VM19-193 reconstructions to an even time step of 3,000 years and use an embedded dimension (window width) $M$ equal to 1/5 the length of the evenly spaced data ($M = 16$). We calculate the singular value decomposition of the $M \times M$ covariance matrix of the centered, evenly spaced data. The eigenvalues from the singular value decomposition are used to quantify the percent of variance explained by each eigenvector. The "reconstructed components"

(RCs) are calculated by projecting the time series onto each mode (see Equation 11 in Ghil et al. (2002) and Equation 1 in Windler et al. (2021)). We determine the combination of leading modes that explains the majority of the variance in each reconstruction and estimate their dominant frequency using a smoothed periodogram (Bloomfield, 2004). We calculate the raw periodogram of each linearly detrended RC and smooth the spectra with an eight-point Gaussian filter.

We perform cross spectral analyses between ETP, or the combination of eccentricity (E), obliquity (tilt; T), and precession (P) (Laskar et al., 2004), and the combined RCs of the leading modes of variability in the new reconstructions from VM19-193, including $\delta D_{precip}$, $\delta^{13}C_{wax}$, SST, and Sub-T, to look at coherence and phase at the different orbital frequency bands. To compare phases of coherent spectral signals in VM19-193 with potential internal drivers, we also perform cross spectral analyses between ETP and the global benthic $\delta^{18}O$ stack (Lisiecki & Raymo, 2005) (representing ice volume) and atmospheric $CO_2$ from the Vostok ice core (Bereiter et al., 2015). All cross spectral analyses were done with the Arand Time Series Analysis Software (Howell et al., 2006). Each record was re-sampled to a consistent time step of 3,000 years prior to analysis and run with 30% lags and a full linear detrend. Precession was weighted by −1 in the ETP record, so that precession minima (NH summer insolation maxima) is phase 0. All isotope proxies (benthic $\delta^{18}O$ stack, $\delta D_{precip}$, and $\delta^{13}C_{wax}$) were multiplied by −1 prior to the cross spectral analysis so that lighter isotope values are in phase with precession minima.

### 2.5. Calculating Glacial Cooling

The changes in the western IO thermocline during glacial periods when the Sunda and Sahul Shelves are exposed may be driven by a dipole-like response to a weaker Walker Circulation over the IO (DiNezio & Tierney, 2013; DiNezio et al., 2016, 2018). To compare glacial changes in the upper water column of the western versus eastern IO during the Late Pleistocene, we calculate overall glacial-to-interglacial changes in the thermocline at VM19-193 consistent with the methodology of Windler et al. (2019b). To do so, we use the ensemble temperature predictions from the BAYSPLINE (SST) and BAYSPAR (Sub-T) calibrations. The range of temperatures from the SST and Sub-T ensembles (2,500 ensemble members for each sample in both the SST and Sub-T records) are sorted from lowest to highest temperature values to retain the structure of the time series. For example, each temperature record ensemble has the dimension $N \times M$, or 94 samples × 2,500 ensemble members, and are sorted along dimension $M$. Sorting in this way retains the shape of the time series when considering all ensembles at once, since the calibrations output temperature values in a random order. To account for the effect of analytical precision on the inferred temperatures, we added uncertainty back into the sorted ensembles: 0.2°C for SST and 0.4°C for Sub-T ($1\sigma$). We define glacial and interglacial periods based on when relative sea level is below (exposed shelf) or above (submerged shelf) −50 m, respectively, using the relative sea level curve from Waelbroeck et al. (2002). The temperature values for the interglacial periods (submerged shelf) are subtracted from the glacial periods (exposed shelf) to calculate the magnitude of glacial cooling in both the SST and Sub-T prediction ensembles. We use a T-test for equality to determine if the distributions of cooling between SST and Sub-T are significantly different (Long & Rippeteau, 1974). We then compare the calculated glacial-interglacial cooling in the SST and Sub-T at VM19-193 with those from MD98-2152 in the eastern IO (Windler et al., 2019b).

## 3. Results

### 3.1. VM19-193 Paleoclimate Reconstructions

Median SSTs largely range from 25 to 30°C over the last 250 ky, except during the Last Glacial Maximum (LGM, 23 ka) when SSTs cooled to 20°C (Figure 4a). There is little visible structure in the SSTs and no pronounced peaks in spectral power at frequencies corresponding to the 23-, 41-, and 100-ky cycles, specifically, frequencies 0.043, 0.024, and 0.01 cycles/ky (Figure 5a). The $U^{K'}_{37}$ values in VM19-193 range from 0.745 to 0.978; therefore, saturation of the $U^{K'}_{37}$ index is not likely to dampen spectral power in the SST record by obscuring warmer temperatures. Median Sub-Ts range from about 16 to 25°C and exhibit larger changes through time than SSTs (Figure 4a). GDGT quality control indices, including the branched and isoprenoidal index (BIT) (Hopmans et al., 2004), the methane index (MI) (Zhang et al., 2011) and the ring index (RI) (Zhang et al., 2016) suggest that pelagic GDGT producers dominated the GDGT pool throughout the span of the record. Average BIT is 0.045 and remains relatively invariant aside from a few data points that approach a value of 0.2. Average MI is 0.24 and does not exceed 0.28. Average ΔRI is 0.07 and never exceeds 0.18. These metrics are available in the data set

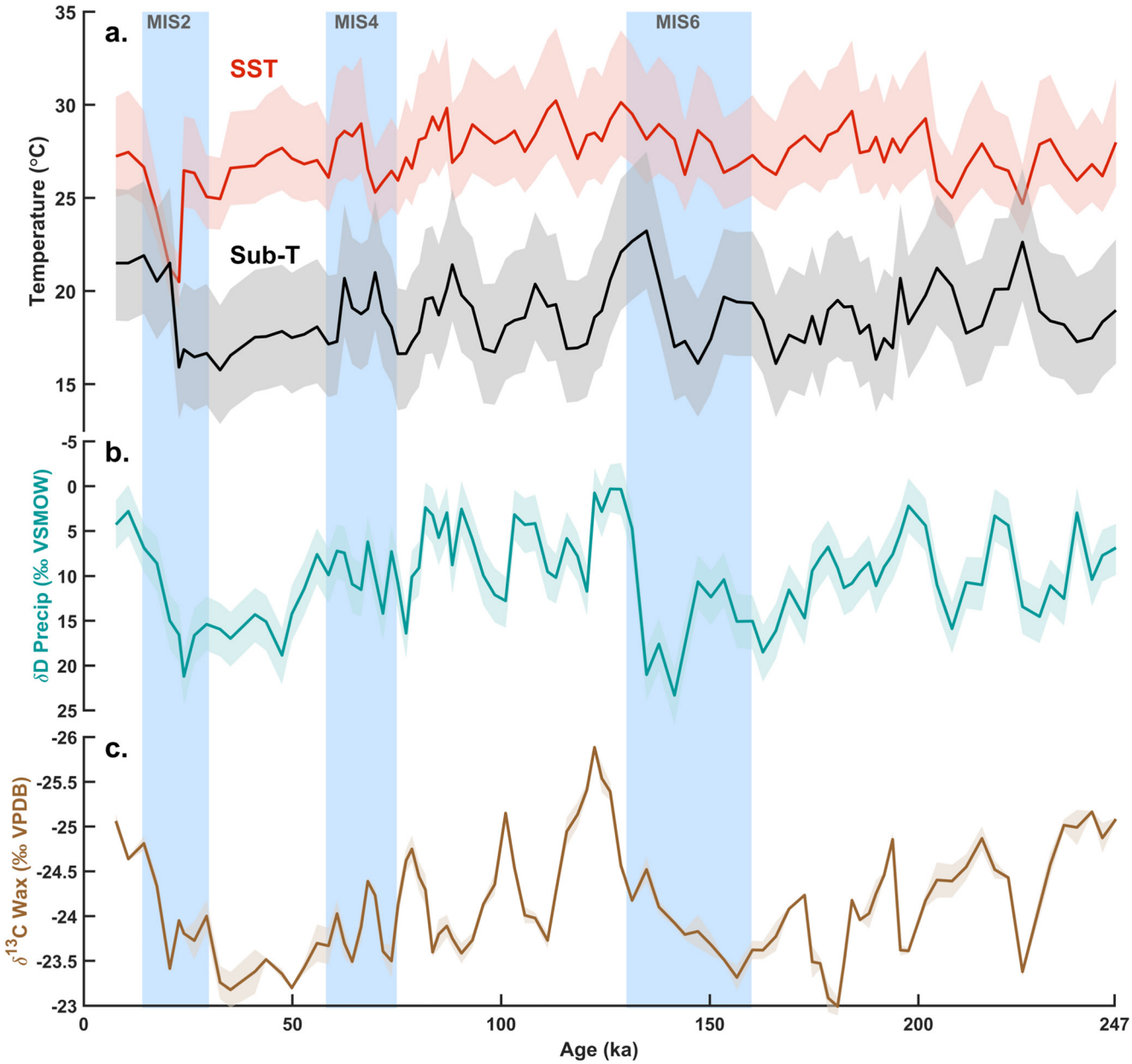


**Figure 4.** Organic proxy reconstructions from VM19-193. (a) sea surface temperature ($U^{K'}_{37}$) and Sub-T ($TEX_{86}$), (b) leaf wax-derived $\delta D_{precip}$, and (c) $\delta^{13}C_{wax}$. Note the reversed *y*-axes in panels b and c. Shading indicates $1\sigma$ uncertainty. Light blue bands denote glacial Marine Isotope Stages.

accompanying this study (Windler et al., 2022). The leading two modes of variability in the Sub-T record explain 52% of the total variance combined and shows peak spectral power at 0.043 cycles/ky, corresponding to the 23 ky precession cycle (Figure 5b). Spectral power at the 100- and 41-ky frequencies is not well defined in the Sub-T record (Figure 5b). Cooling during glacial periods, when the Sunda and Sahul Shelves are exposed, over the last 250 ky is −0.9°C in the surface with more widely distributed estimates than Sub-T, which cooled approximately −0.4°C during shelf exposure (Figure 6a).

The $\delta D_{precip}$ values range from −4 to +23 ‰ and display more glacial-interglacial structure than the temperature records, with more enriched values occurring during glacial periods at ∼25 and 140 ka (Figure 4b). The difference between glacial and interglacial extremes in $\delta D_{precip}$ approaches 20‰ for the transitions between MIS 6/5 and MIS 2/1. The $\delta D_{precip}$ has pronounced peaks in spectral power at frequencies corresponding to the 23 ky precession cycle (27% of the variance) and the 100 ky cycle (up to 46% of the variance between modes 1 and

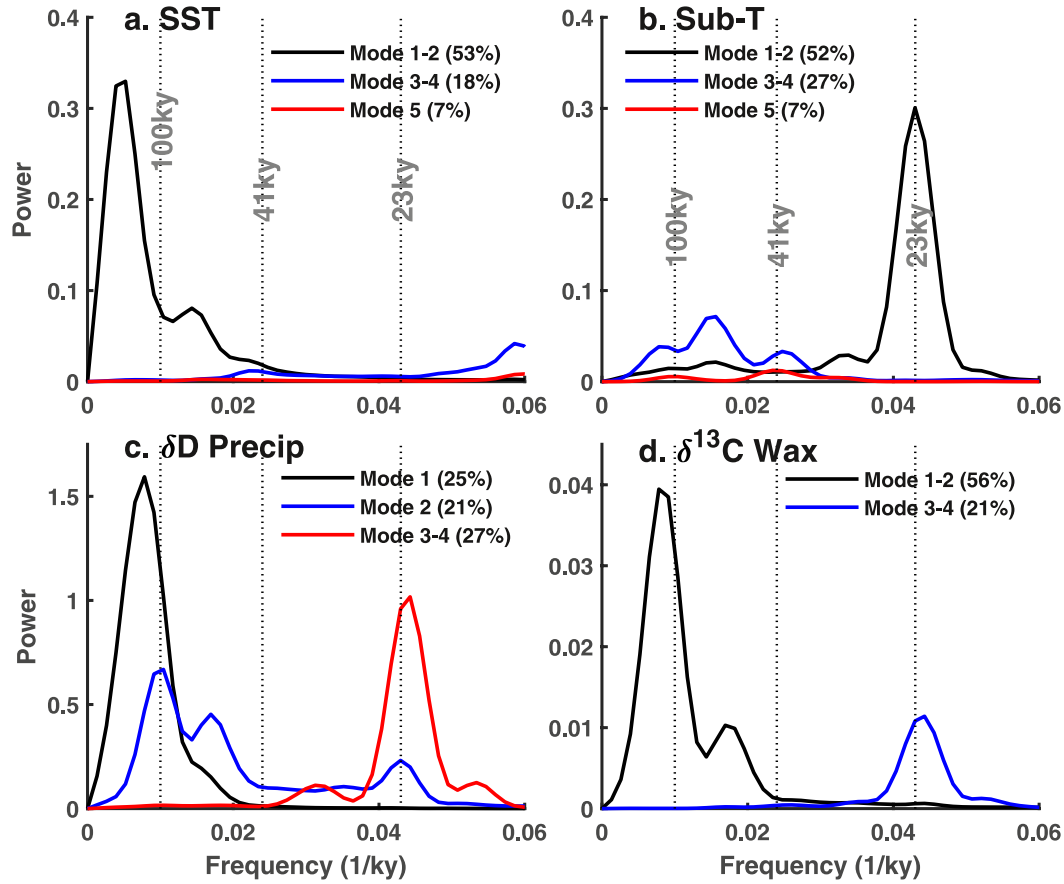


**Figure 5.** Smoothed periodograms of leading modes from the singular spectrum analysis for VM19-193 reconstructions. (a) sea surface temperature, (b) Sub-T, (c) $\delta D_{precip}$, and (d) $\delta^{13}C_{wax}$. The 23-, 41-, and 100-ky orbital frequencies are marked with dotted lines in each panel. Modes in quadrature (modes that have similar but out-of-phase empirical orthogonal functions and the same frequency (Ghil et al., 2002)) are combined and listed as pairs. Explained variance for each mode are listed in parentheses.

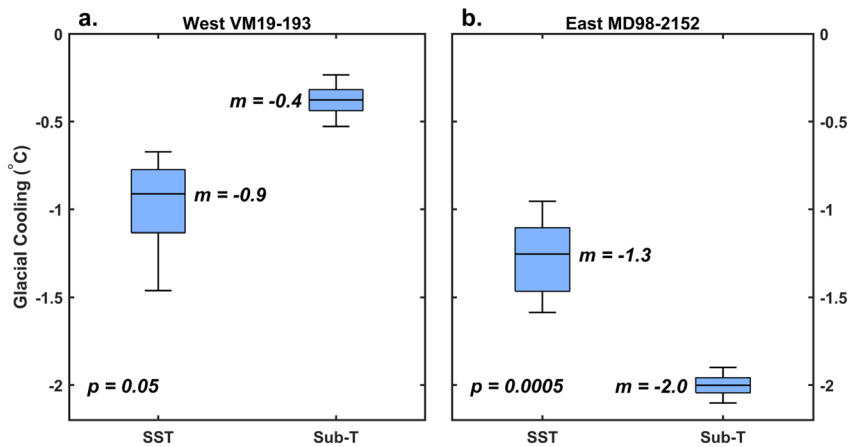


**Figure 6.** Distributions of the amount of cooling of sea surface temperature (SST) versus Sub-T between glacial periods of shelf exposure and interglacial periods when the shelf is submerged at (a) VM19-193 in the western IO from this study (Windler et al., 2022) and (b) MD98-2152 in the eastern IO from Windler et al. (2019b). Box whiskers represent the 5% and 95% confidence levels. Box lines represent median values, which are listed. The p-values from the T-tests between the distributions of cooling in SST and Sub-T records at each location are also listed. A p-value <0.05 indicates the distributions are significantly different.

**Table 2**
*Coherency and Phase Results From Cross Spectral Analyses at Orbital Frequency Bands for the VM19-193 Reconstructions (This Study), Ice Volume Minima (Lisiecki & Raymo, 2005), and $CO_2$ Concentrations (Bereiter et al., 2015) All Relative to ETP*

| | Precession (23 ky) | | Obliquity (41 ky) | | Eccentricity (100 ky) | |
|---|---|---|---|---|---|---|
| Reconstruction | Coherency | Phase ± 1$\sigma$ | Coherency | Phase ± 1$\sigma$ | Coherency | Phase ± 1$\sigma$ |
| $\delta D_{precip}$ Min | 0.97 | −13° ± 7 | 0.30 | – | 0.91 | −27° ± 12 |
| $\delta^{13}C_{wax}$ Min | 0.88 | −91° ± 14 | 0.21 | – | 0.84 | +38° ± 16 |
| SST Max | 0.22 | – | 0.36 | – | 0.62 | – |
| Sub-T Max | 0.94 | +61° ± 9 | 0.72 | +20° ± 23 | 0.77 | +37° ± 21 |
| Ice Min | 0.85 | −78° ± 16 | 0.88 | −70° ± 14 | 0.89 | −6° ± 13 |
| $CO_2$ Max | 0.78 | −71° ± 20 | 0.74 | −70° ± 22 | 0.84 | +5° ± 16 |

*Note*. Coherency above 0.64 and 0.79 are significant above noise at the 80% and 95% confidence levels, respectively. Phase values are only listed if the proxy is coherent at that frequency band. Negative phase values indicate lag and positive phase values indicate lead.

2; Figure 5c). The $\delta^{13}C_{wax}$ values range from only −23 to −26 ‰ (Figure 4c) and are indicative of large contributions from $C_4$ grasses to this location (Figure S2 in Supporting Information S1) reflecting the grass savannah landscape east of the Kenyan and Ethiopian highlands (Schefuß et al., 2003). The $\delta^{13}C_{wax}$ record has strong spectral power at the 100 ky cycle (56% of the total variance) and a secondary component that peaks at the 23 ky precession cycle (21% of the variance; Figure 5d).

### 3.2. Cross Spectral Phases Relative to ETP

Coherence and phase are used to describe the correlation and timing between different time series at particular frequency bands. Here, we report the coherence and phase of the RCs of leading modes of variability of each reconstruction relative to ETP at the precession (23 ky), obliquity (41 ky), and 100 ky frequency bands (Table 2). Phase wheels are useful for summarizing the phase relationships (relative timing) of proxy reconstructions to either external drivers of climate such as the amount of insolation, or internal drivers such as global ice volume or greenhouse gases (Figure 7). For instance, ice volume minima (ice) and atmospheric $CO_2$ concentrations are well known internal drivers of Earth's climate during the Pleistocene (Bereiter et al., 2015; Lisiecki & Raymo, 2005). Both are coherent with ETP at all three orbital frequency bands and lag precession minima (June 21 perihelion) (Table 2). Our cross spectral results for ice and $CO_2$ are comparable to those reported in other studies (Bolton et al., 2013; S. C. Clemens et al., 2021; McGrath et al., 2021).

The Sub-T, $\delta D_{precip}$, and $\delta^{13}C_{wax}$ reconstructions from VM19-193 are all coherent with ETP at the 23 ky precessional frequency band (Table 2, Figure 7), so we focus our phase discussion below on precession. Positive phase values indicate lead and plot to the left on the phase wheel, whereas negative phase values indicate lag from the zero phase (in this case June 21 perihelion) and plot to the right on the phase wheel. Among the VM19-193 reconstructions, only Sub-T is coherent with ETP at the obliquity frequency band. Sub-T, $\delta D_{precip}$, and $\delta^{13}C_{wax}$ are coherent at the eccentricity band (Table 2). As a point of comparison, we perform a SSA and cross spectral analysis using the same methodology described above for $\delta D_{precip}$ and $\delta^{13}C_{wax}$ from the Gulf of Aden (RC09-166 in Figure 1) (Tierney et al., 2017a). See Figures S3 and S4 in Supporting Information S1.

## 4. Discussion

### 4.1. Precessional Variability

The leaf wax reconstructions ($\delta D_{precip}$ and $\delta^{13}C_{wax}$) both display a peak in spectral power at the 23 ky precession frequency (Figures 5c and 5d), but are almost 90° out-of-phase with one another (Figure 7). The $\delta D_{precip}$ plots close to zero-phase within uncertainty (Table 2), indicating that the primary driver of $\delta D_{precip}$ over the equatorial east African coast is precession minima, or NH summer insolation maxima (Figure 7). By contrast, $\delta^{13}C_{wax}$ is in phase with insolation maxima during NH fall within uncertainty (Figure 7). In other words, $\delta D_{precip}$ is lighter

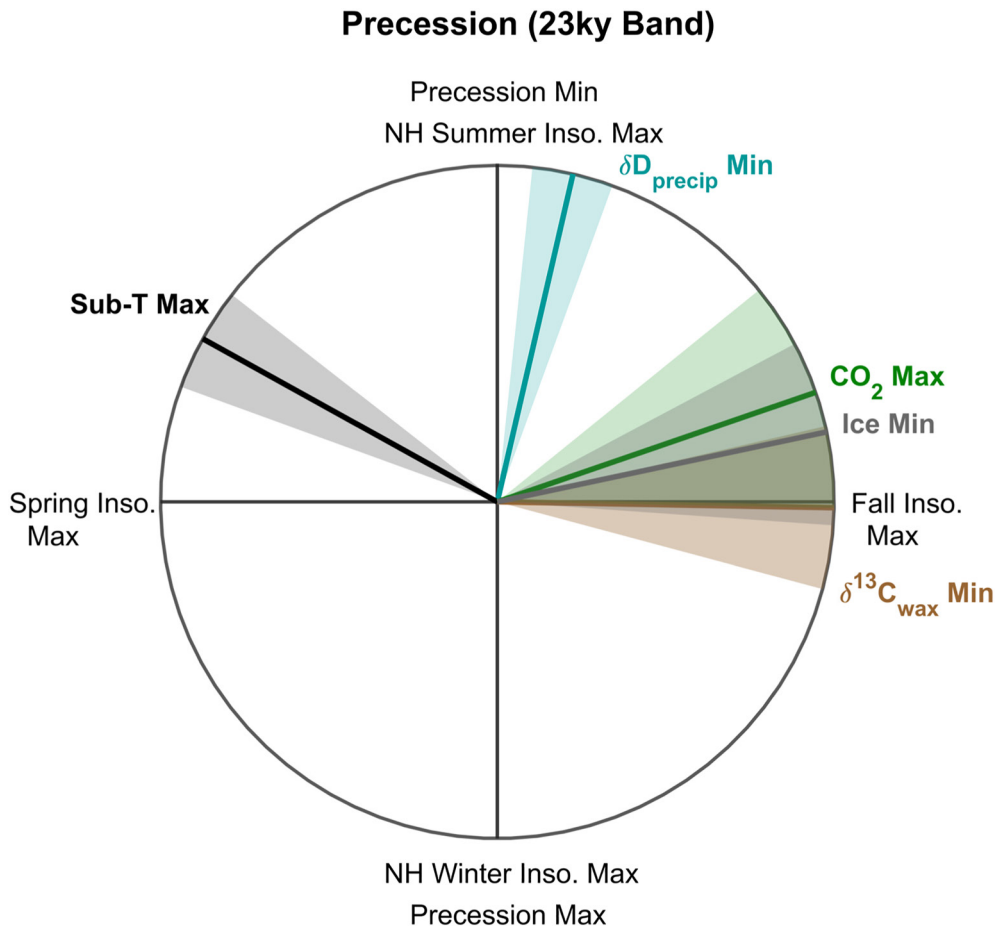


**Figure 7.** Phase relationships of the VM19-193 reconstructions (this study), ice volume minima (Lisiecki & Raymo, 2005), and $CO_2$ concentration (Bereiter et al., 2015) all relative to ETP at the precession frequency band. All isotope proxy records ($\delta D_{precip}$, $\delta^{13}C_{wax}$, and the benthic $\delta^{18}O$ stack) were multiplied by −1 so that lighter isotope values are in phase with precession minima (June 21 perihelion). All plotted phases exceed the 95% confidence level of non-zero coherency reported in Table 2. Negative (positive) phase values indicate a lag (lead) between the proxy and phase 0, which plots to the right (left) of the top of the wheel. Error bars represent 1$\sigma$ uncertainties.

(more depleted in D) in response to insolation maxima during NH summer and $\delta^{13}C_{wax}$ is lighter (more $C_3$ plant material) following NH fall insolation maxima. This ~90° phase contrast suggests that the different leaf wax isotopes in this region are recording distinct signals.

Equatorial east Africa receives most of its precipitation during either the NH spring "long rains," or the "short rains" during the fall (Figure 2b), thereby driving the vegetation growing season during those times. The coherency of $\delta^{13}C_{wax}$ with NH fall insolation over precessional cycles (Figure 7) suggests that variability in the fall season "short rains" is dominating the precessional-scale local precipitation signal in this region. In other words, the relative amount of $C_3$ and $C_4$ vegetation recorded by $\delta^{13}C_{wax}$ is responding to changes in the fall rainy season over equatorial east Africa. In line with this, coupled simulations for the mid-Holocene (6 ka)—a time with maximum insolation during NH fall (Laskar et al., 2004)—indicate rainfall increases from June to November, and decreases from December to May, over the western IO and equatorial east Africa (LeGrande & Schmidt, 2009; Tierney et al., 2011). Our results indicate that this simulated change in rainfall seasonality is likely a consistent feature during the precessional cycles of the last 250 ky: increases in NH fall insolation result in increased precipitation during the fall "short rains" season, likely due to enhanced local convection, over the arid savannah grasslands of equatorial eastern-most Africa, which allows for the landscape to support an expansion of $C_3$ plants during the fall growing season. Changes in $CO_2$ are small over precessional time scales and so are not likely to impact vegetation at this frequency, making a vegetation response to localized rainfall availability a reasonable mechanism for driving $\delta^{13}C_{wax}$ changes at this location.

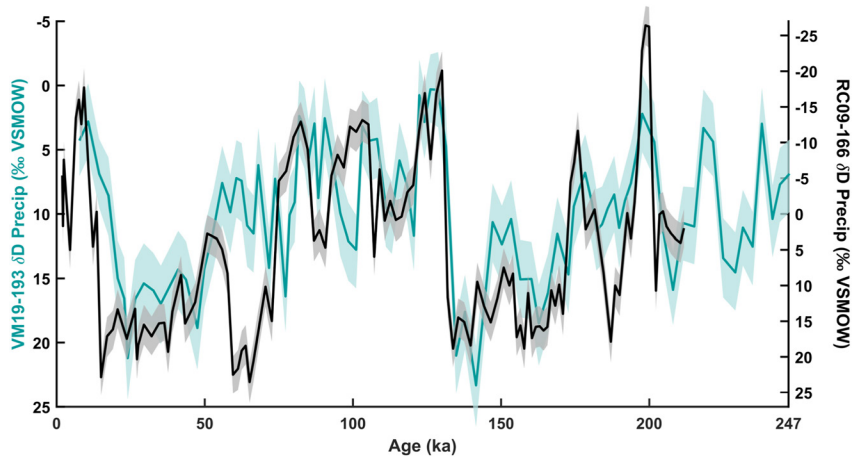


**Figure 8.** Reconstructions of $\delta D_{precip}$ from VM19-193 (blue line) (Windler et al., 2022) and RC09-166 (black line) (Tierney et al., 2017a). Shading represents $1\sigma$ uncertainty. The $\delta D_{precip}$ of RC09-166 was calculated from $\delta D_{wax}$ values using the same methodology described in this study.

Contrary to the local NH fall season precipitation signal captured by the carbon isotope composition of the vegetation on the landscape, the $\delta D_{precip}$ from this area likely reflects large-scale regional circulation changes associated with the summer monsoon. The maximum NH summer insolation that occurs during precession minima more rapidly heats up the NH land surface in early summer, increasing the land-sea temperature contrast, and causing the loci of heavy monsoon precipitation to shift northward. Idealized modeling experiments have found that this northward shift increases summer precipitation over northeast Africa, the Arabian Peninsula, and southern Asia when NH insolation is high (Battisti et al., 2014; Bosmans et al., 2018). Isotope-enabled simulations estimate a similar spatial pattern in the isotopic composition of precipitation; however, the lighter precipitation isotope values under high insolation are driven by large-scale transport of depleted water vapor rather than the amount of local precipitation (Battisti et al., 2014). Summer rainfall over equatorial east Africa and the Horn of Africa does not change much during precession minima (Battisti et al., 2014; Bosmans et al., 2018), but $\delta D_{precip}$ from VM19-193 suggests that this area was affected by intensified monsoon circulation over precessional time scales.

The lighter $\delta D_{precip}$ values in VM19-193 during high NH summer insolation could be specifically related to low-level moisture convergence over the tropical western IO from an intensified Somali Jet. Bosmans et al. (2018) simulated a dipole-like response in NH summer across the tropical IO during precession minima: enhanced easterly winds across the southern IO lead to warmer SSTs, lower sea level pressure, and increased precipitation and upward motion of air over the equatorial western IO. Converging moisture at low levels of the atmosphere is isotopically depleted relative to local moisture sources because it retains the rainout of heavy isotopes along its trajectory (Aggarwal et al., 2012; Galewsky et al., 2016; Moore et al., 2014). Today, summer is relatively dry in east Africa, but still receives some rainfall (Figure 2b). The summer depletion signal from enhanced monsoon circulation must have been large enough to either dominate the $\delta D_{precip}$ values from the rest of the year, or carry over into the fall growing season.

Either way, the VM19-193 leaf wax record refines our understanding of the drivers of $\delta D_{precip}$ in east Africa. The almost 90°phase offset between $\delta D$ and $\delta^{13}C$ clearly suggests that each isotope system is recording a different seasonal aspect of the regional hydrological cycle. Previous work has argued that $\delta D_{precip}$ over the Horn of Africa region reflects aridity (Tierney & DeMenocal, 2013; Tierney et al., 2017a), whereas the results here suggest it is more accurately understood as a summer monsoon circulation indicator. Changes in circulation have consequences for aridity insofar as they may be associated with an increase or decrease in summer rainfall, so these interpretations are not mutually exclusive; however, circulation provides a better explanation for the similarities between VM19-193 and other records of $\delta D_{precip}$ from east Africa (i.e., (Tierney & DeMenocal, 2013)) that are ca. 1,000 km distant. Indeed, the VM19-193 $\delta D_{precip}$ record is similar to $\delta D_{precip}$ from RC09-166 in the Gulf of Aden for the last 200 ky (Figure 8) (Tierney et al., 2017a) in line with the regionally coherent changes in precipitation isotopes simulated in Battisti et al. (2014). The precessional phasing of RC09-166 is likewise close to zero phase within uncertainty (Figure S4 in Supporting Information S1). The only substantial difference between the records

is during MIS 4, when RC09-166 exhibits much more enriched isotopes than VM19-193 (Figure 8). This could reflect a real regional difference in hydroclimate, representing a particularly dry period focused within the Horn region that corresponds with a major "out-of-Africa" human migration event (Tierney et al., 2017a).

The Sub-T reconstruction at VM19-193 is coherent with ETP above the 95% confidence level at the precession band (Table 2) and plots between insolation maxima during NH spring and summer on the phase wheel, closer to spring maxima (Figure 7). This phasing of the Sub-T record suggests that the amount of heating during the spring season, when local insolation is highest (Figure 2b) is a dominant control on mean annual upper water column temperatures at this equatorial site. In other words, during periods of NH spring insolation maxima, the seasonal insolation cycle observed today (Figure 2b) is enhanced, leading to greater heating of the upper water column during the spring season at this location that is apparently not counter-balanced by cooling in other times of the year.

In contrast with the Sub-T record, the alkenone SST data show no coherency with ETP in the precessional band (Table 2) and there is no evidence of spectral power near precession in the SSA results (Figure 5a). This suggests that precessional forcing of SST is symmetric across the seasonal cycle (i.e., warming during one season is counterbalanced by cooling during a different season) leading to a net-zero impact on mean-annual SST variability.

### 4.2. Glacial-Interglacial Variability

VM19-193 is ideally located to test the western IO response to glacial shelf exposure over the Maritime Continent in the eastern IO Basin. The shelf exposure mechanism asserts that during glacial periods, when sea level is low relative to today, the exposed Sunda and Sahul Shelves in the Indo-Pacific region cool the surface via increased albedo relative to the surrounding ocean (DiNezio & Tierney, 2013; DiNezio et al., 2016). This surface cooling causes a decoupling of the Indian (weaker) and Pacific (stronger) Walker Circulation cells (DiNezio et al., 2016, 2018). Weaker circulation over the tropical eastern IO leads to increased low level moisture divergence (Windler et al., 2020) and a dipole-like mean state where anomalous easterly winds become part of a positive feedback with a warmer west/cooler east SST gradient, causing upwelling off the Sumatra and Java coasts (DiNezio et al., 2016, 2018). Increased convection over the warmer SSTs (and deeper thermocline) in the western IO also contribute to a precipitation dipole, where rainfall increases over the ocean and east African coastline and severe drying across the Sunda Shelf in the eastern IO (DiNezio & Tierney, 2013; DiNezio et al., 2016, 2018).

A comparison of SST and Sub-T reconstructions from core MD98-2152 off southern Sumatra (Figure 6b) agrees with the simulated dipole-like response to shelf exposure, where Sub-Ts show greater cooling when the shelves are exposed than SSTs, indicating upwelling in the equatorial eastern IO driven by sea level (Figure 6b) (Windler et al., 2019b). Our results for VM19-193 show that the Sub-Ts in the tropical western IO experience very little glacial cooling during the last 250 ky, whereas SSTs cool slightly more, though there is not a significant difference between the two (Figure 6a). In other words, the thermocline is getting deeper or experiencing very little change over glacial-interglacial time scales in the tropical western IO. This supports shelf exposure as a primary mechanism influencing climate in the IO Basin during glacial periods. A direct comparison of the eastern and western temperature reconstructions is shown in Figure S5 in Supporting Information S1. Why then, do neither the SST, nor Sub-T records show prominent spectral power at the 100 ky frequency (Figures 5a and 5b)? This lack of 100 ky power is likely canceled out by the overall cooler conditions of glacial periods. For example, if the entire IO cooled by ~3°C during MIS 6, but the feedbacks associated with shelf exposure made the tropical western IO warmer relative to the rest of the basin, then the overall cooling effect of glacial conditions is counteracted by the effect of shelf exposure at this location. The result is muted glacial variability in the temperature proxies.

Since the $\delta^{13}C_{wax}$ from VM19-193 represents a vegetation response to local precipitation over precessional time scales, then we might expect the 100 ky spectral power in the record (Figure 5d) to vary according to the shelf exposure mechanism, which instigates a rainfall dipole across the tropical IO with a wetter western IO and a drier eastern IO (DiNezio et al., 2016, 2018). Regional vegetation over southern Sumatra and western Java shows an expansion of $C_4$ grassland during glacial periods of the last 450 ky, indicating enhanced rainfall seasonality with a more intense dry season associated with weaker IO Walker Circulation (Windler et al., 2019b); however, $\delta^{13}C_{wax}$ from VM19-193 does not indicate a wetter east African coastline during the glacial periods MIS 2 and 6 (Figure 4c). The glacial response of $\delta^{13}C_{wax}$ from equatorial east Africa suggests that the increase in rainfall associated with shelf exposure may have been limited to the ocean, where the largest changes are simulated (DiNezio et al., 2016, 2018; DiNezio & Tierney, 2013).

Additionally, the 100 ky variability in $\delta^{13}C_{wax}$ may be reflecting $CO_2$ limitations on the vegetation. Lower atmospheric $CO_2$ concentrations mean that $C_4$ grasses have an advantage over $C_3$ plants under glacial conditions (Ehleringer et al., 1997; Sachse et al., 2012), thus limiting $C_3$ expansion over the landscape. The $\delta^{13}C_{wax}$ record is coherent with ETP at the 100 ky frequency band above the 95% level; however, phase values suggest that $\delta^{13}C_{wax}$ leads changes in $CO_2$ (Table 2). The difference in dating between the records, the small number of full glacial cycles represented by VM19-193, and the high phase errors make this relationship difficult to quantify in this study; however, a new $\delta^{13}C_{wax}$ record of northwest African vegetation changes shows that the relative changes in $C_3/C_4$ plant distribution closely tracks $CO_2$ concentrations over 100 ky time scales, not ice volume (O'Mara et al., 2022).

The prominent 100 ky spectral power in the $\delta D_{precip}$ from VM19-193 (Figure 5c) is notable, as it suggests a broad reorganization of circulation related to a weaker Afro-Indian monsoon system during glacial periods. Strong 100 ky variability has also been found in precipitation isotope reconstructions from the Gulf of Aden (Figure S3 in Supporting Information S1) (Tierney et al., 2017a) and regions affected by the Indian and East Asian summer monsoons (McGrath et al., 2021; Windler et al., 2021) with the exception being speleothems from eastern China, the interpretations of which are highly debated (Cheng et al., 2016; Chiang et al., 2015; S. C. Clemens et al., 2010, 2018; Liu et al., 2014; Wang et al., 2001). The presence of 100 ky power in different precipitation isotope archives across the different monsoon regions adjacent to the IO suggests a spatially coherent summer monsoon response to glacial climates.

Simulations of glacial conditions have found widespread reductions in summer precipitation from Africa to northwest India, which may be driven by mid-latitude advection of cold, dry air via the westerlies that mixes equatorward and limits the spatial extent of the summer monsoon into the Asian continent (DiNezio et al., 2018). Weaker monsoon circulation would likely shorten moisture transport resulting in the observed precipitation isotopic enrichment over the region (Y. Cai et al., 2015; McGrath et al., 2021; Moore et al., 2014). No matter the exact mechanism, the pronounced glacial-interglacial changes in $\delta D_{precip}$ (Figure 4b) indicate that equatorial east African hydroclimate responds to glacial boundary conditions (i.e., extensive NH ice sheets and/or reduced greenhouse gas concentrations). Additionally, the 100 ky variability in RC09-166 (Figure S3 in Supporting Information S1) suggests that northeast Africa responds to similar mechanisms over glacial-interglacial time scales. This directly contrasts with west African dust and vegetation records that suggest the African monsoon system is a purely precessional signal that is coherent throughout the late Pleistocene (Kuechler et al., 2013; O'Mara et al., 2022; Skonieczny et al., 2019). Future work is necessary to reconcile this spectral difference over the African continent.

## 5. Conclusions

We have presented four new climate reconstructions from the tropical western IO that span the last 250 ky. We found strong 23 ky precessional variability in marine Sub-Ts, the $\delta$D of precipitation, and the $\delta^{13}$C of regional vegetation from east Africa that all exhibit different phasing with respect to NH summer insolation maxima during this period. Sub-Ts are likely driven primarily by NH spring insolation maxima, which exacerbates the modern seasonal insolation cycle at this location. Despite this spring-driven signal in the ocean, vegetation shifts follow local rainfall over equatorial east Africa during the NH fall "short rains." The $\delta D_{precip}$ more closely follows NH summer insolation maxima over precessional time scales, likely reflecting large regional circulation changes associated with summer monsoon intensity.

We expect the lack of a 100 ky spectral signal in the temperature reconstructions if the shelf exposure mechanism is influencing the equatorial western IO during glacial climates: the warming from shelf exposure works in opposition to overall glacial cooling. Our calculation of glacial cooling in the SST and Sub-T records from the western IO indicate that the sub-surface cooled less than the surface (deeper thermocline), which supports shelf exposure over the Maritime Continent as a primary mechanism influencing glacial-interglacial climate variability in the IO; however the $\delta^{13}C_{wax}$ sourced from equatorial east Africa do not show expansion of $C_3$ plants over the landscape during glacial periods. This may indicate that the rainfall dipole associated with shelf exposure was limited to the open ocean. By contrast, the 100 ky signal in $\delta D_{precip}$ from the tropical western IO may reflect a spatially coherent weaker monsoon circulation across the IO Basin during glacial periods. Overall, the VM19-193 record of hydroclimate over east Africa indicates that both precession and glacial-interglacial cycles play key roles in driving ocean-atmosphere responses to climate at this tropical location.

## Data Availability Statement

The VM19-193 data generated in this study are available from NOAA's National Centers for Environmental Information (Windler et al., 2022). The temperature reconstructions from MD98-2152 are available through Windler et al. (2019a). The leaf wax data from RC09-166 are available through Tierney et al. (2017b).

**Acknowledgments**
Funding for this study was provided by the David and Lucile Packard Foundation Fellowship in Science and Engineering to J.E. Tierney and by the National Science Foundation Graduate Research Fellowship Program to G. Windler (Grant DGE-1746060). The authors would like to thank P. Murphy for technical support, K. Thirumalai for cross spectral analysis and phase wheel guidance, and S. McGrath for additional technical cross spectral support.

## References

Aggarwal, P. K., Alduchov, O. A., Froehlich, K. O., Araguas-Araguas, L. J., Sturchio, N. C., & Kurita, N. (2012). Stable isotopes in global precipitation: A unified interpretation based on atmospheric moisture residence time. *Geophysical Research Letters*, *39*(11), L11705. https://doi.org/10.1029/2012gl051937

Allen, M. R., & Smith, L. A. (1996). Monte Carlo SSA: Detecting irregular oscillations in the presence of colored noise. *Journal of Climate*, *9*(12), 3373–3404. https://doi.org/10.1175/1520-0442(1996)009<3373:mcsdio>2.0.co;2

Allen, M. R., & Smith, L. A. (1997). Optimal filtering in singular spectrum analysis. *Physics Letters* A, *234*(6), 419–428. https://doi.org/10.1016/s0375-9601(97)00559-8

Alory, G., Wijffels, S., & Meyers, G. (2007). Observed temperature trends in the Indian Ocean over 1960–1999 and associated mechanisms. *Geophysical Research Letters*, *34*(2), L02606. https://doi.org/10.1029/2006gl028044

Anderson, D. M., & Prell, W. L. (1993). A 300 kyr record of upwelling off Oman during the late Quaternary: Evidence of the Asian southwest monsoon. *Paleoceanography*, *8*(2), 193–208. https://doi.org/10.1029/93pa00256

Battisti, D., Ding, Q., & Roe, G. (2014). Coherent pan-Asian climatic and isotopic response to orbital forcing of tropical insolation. *Journal of Geophysical Research: Atmospheres*, *119*(21), 11–997. https://doi.org/10.1002/2014jd021960

Bereiter, B., Eggleston, S., Schmitt, J., Nehrbass-Ahles, C., Stocker, T. F., Fischer, H., et al. (2015). Revision of the EPICA Dome C CO2 record from 800 to 600 kyr before present. *Geophysical Research Letters*, *42*(2), 542–549. https://doi.org/10.1002/2014gl061957

Bhattacharya, T., Tierney, J. E., Addison, J. A., & Murray, J. W. (2018). Ice-sheet modulation of deglacial North American monsoon intensification. *Nature Geoscience*, *11*(11), 848–852. https://doi.org/10.1038/s41561-018-0220-7

Bloomfield, P. (2004). *Fourier analysis of time series: An introduction*. John Wiley & Sons.

Bolton, C. T., Chang, L., Clemens, S. C., Kodama, K., Ikehara, M., Medina-Elizalde, M., et al. (2013). A 500,000 year record of Indian summer monsoon dynamics recorded by eastern equatorial Indian Ocean upper water-column structure. *Quaternary Science Reviews*, *77*, 167–180. https://doi.org/10.1016/j.quascirev.2013.07.031

Bosmans, J., Erb, M., Dolan, A., Drijfhout, S., Tuenter, E., Hilgen, F., et al. (2018). Response of the Asian summer monsoons to idealized precession and obliquity forcing in a set of GCMs. *Quaternary Science Reviews*, *188*, 121–135. https://doi.org/10.1016/j.quascirev.2018.03.025

Brassell, S. C., Eglinton, G., Marlowe, I., Pflaumann, U., & Sarnthein, M. (1986). Molecular stratigraphy: A new tool for climatic assessment. *Nature*, *320*(6058), 129–133. https://doi.org/10.1038/320129a0

Bronk Ramsey, C. (2008). Deposition models for chronological records. *Quaternary Science Reviews*, *27*(1–2), 42–60. https://doi.org/10.1016/j.quascirev.2007.01.019

Cai, W., Santoso, A., Wang, G., Weller, E., Wu, L., Ashok, K., et al. (2014). Increased frequency of extreme Indian Ocean dipole events due to greenhouse warming. *Nature*, *510*(7504), 254–258. https://doi.org/10.1038/nature13327

Cai, Y., Fung, I. Y., Edwards, R. L., An, Z., Cheng, H., Lee, J.-E., et al. (2015). Variability of stalagmite-inferred Indian monsoon precipitation over the past 252,000 y. *Proceedings of the National Academy of Sciences of the United States of America*, *112*(10), 2954–2959. https://doi.org/10.1073/pnas.1424035112

Chen, W., Mohtadi, M., Schefuß, E., & Mollenhauer, G. (2016). Concentrations and abundance ratios of long-chain alkenones and glycerol dialkyl glycerol tetraethers in sinking particles south of Java. *Deep Sea Research Part I: Oceanographic Research Papers*, *112*, 14–24. https://doi.org/10.1016/j.dsr.2016.02.010

Cheng, H., Edwards, R. L., Sinha, A., Spötl, C., Yi, L., Chen, S., et al. (2016). The Asian monsoon over the past 640,000 years and ice age terminations. *Nature*, *534*(7609), 640–646. https://doi.org/10.1038/nature18591

Chiang, J. C., Fung, I. Y., Wu, C.-H., Cai, Y., Edman, J. P., Liu, Y., et al. (2015). Role of seasonal transitions and westerly jets in East Asian paleoclimate. *Quaternary Science Reviews*, *108*, 111–129. https://doi.org/10.1016/j.quascirev.2014.11.009

Church, M. J., Wai, B., Karl, D. M., & DeLong, E. F. (2010). Abundances of crenarchaeal amoa genes and transcripts in the Pacific Ocean. *Environmental Microbiology*, *12*(3), 679–688. https://doi.org/10.1111/j.1462-2920.2009.02108.x

Clemens, S., Prell, W., Murray, D., Shimmield, G., & Weedon, G. (1991). Forcing mechanisms of the Indian Ocean monsoon. *Nature*, *353*(6346), 720–725. https://doi.org/10.1038/353720a0

Clemens, S. C., Holbourn, A., Kubota, Y., Lee, K., Liu, Z., Chen, G., et al. (2018). Precession-band variance missing from East Asian monsoon runoff. *Nature Communications*, *9*(1), 1–12. https://doi.org/10.1038/s41467-018-05814-0

Clemens, S. C., & Prell, W. L. (2003). A 350,000 year summer-monsoon multi-proxy stack from the Owen Ridge, northern Arabian Sea. *Marine Geology*, *201*(1–3), 35–51. https://doi.org/10.1016/s0025-3227(03)00207-x

Clemens, S. C., Prell, W. L., & Sun, Y. (2010). Orbital-scale timing and mechanisms driving late Pleistocene Indo-Asian summer monsoons: Reinterpreting cave speleothem $\delta^{18}$O. *Paleoceanography*, *25*(4). https://doi.org/10.1029/2010pa001926

Clemens, S. C., Yamamoto, M., Thirumalai, K., Giosan, L., Richey, J. N., Nilsson-Kerr, K., et al. (2021). Remote and local drivers of Pleistocene south Asian summer monsoon precipitation: A test for future predictions. *Science Advances*, *7*(23), eabg3848. https://doi.org/10.1126/sciadv.abg3848

Clement, A. C., Hall, A., & Broccoli, A. (2004). The importance of precessional signals in the tropical climate. *Climate Dynamics*, *22*(4), 327–341. https://doi.org/10.1007/s00382-003-0375-8

Conte, M. H., Sicre, M.-A., Rühlemann, C., Weber, J. C., Schulte, S., Schulz-Bull, D., & Blanz, T. (2006). Global temperature calibration of the alkenone unsaturation index (UK 37) in surface waters and comparison with surface sediments. *Geochemistry, Geophysics, Geosystems*, *7*(2). https://doi.org/10.1029/2005gc001054

DiNezio, P. N., Puy, M., Thirumalai, K., Jin, F.-F., & Tierney, J. E. (2020). Emergence of an equatorial mode of climate variability in the Indian Ocean. *Science Advances*, *6*(19), eaay7684. https://doi.org/10.1126/sciadv.aay7684

DiNezio, P. N., & Tierney, J. E. (2013). The effect of sea level on glacial Indo-Pacific climate. *Nature Geoscience*, *6*(6), 485–491. https://doi.org/10.1038/ngeo1823

DiNezio, P. N., Tierney, J. E., Otto-Bliesner, B. L., Timmermann, A., Bhattacharya, T., Rosenbloom, N., & Brady, E. (2018). Glacial changes in tropical climate amplified by the Indian Ocean. *Science Advances*, *4*(12), eaat9658. https://doi.org/10.1126/sciadv.aat9658

DiNezio, P. N., Timmermann, A., Tierney, J. E., Jin, F.-F., Otto-Bliesner, B., Rosenbloom, N., et al. (2016). The climate response of the Indo-Pacific Warm Pool to glacial sea level. *Paleoceanography*, *31*(6), 866–894. https://doi.org/10.1002/2015pa002890

Divakar Naidu, P., Malmgren, B. A., & Bornmalm, L. (1993). Quaternary history of calcium carbonate fluctuations in the western equatorial Indian Ocean (Somali basin). *Palaeogeography, Palaeoclimatology, Palaeoecology*, *103*(1–2), 21–30. https://doi.org/10.1016/0031-0182(93)90048-n

Eglinton, G., & Hamilton, R. J. (1967). Leaf epicuticular waxes. *Science*, *156*(3780), 1322–1335. https://doi.org/10.1126/science.156.3780.1322

Eglinton, T. I., & Eglinton, G. (2008). Molecular proxies for paleoclimatology. *Earth and Planetary Science Letters*, *275*(1–2), 1–16. https://doi.org/10.1016/j.epsl.2008.07.012

Ehleringer, J. R., Cerling, T. E., & Helliker, B. R. (1997). C4 photosynthesis, atmospheric CO2, and climate. *Oecologia*, *112*(3), 285–299. https://doi.org/10.1007/s004420050311

Feakins, S. J., Eglinton, T. I., & demenocal, P. B. (2007). A comparison of biomarker records of northeast African vegetation from lacustrine and marine sediments (ca. 3.40 Ma). *Organic Geochemistry*, *38*(10), 1607–1624. https://doi.org/10.1016/j.orggeochem.2007.06.008

Feakins, S. J., & Sessions, A. L. (2010). Controls on the D/H ratios of plant leaf waxes in an arid ecosystem. *Geochimica et Cosmochimica Acta*, *74*(7), 2128–2141. https://doi.org/10.1016/j.gca.2010.01.016

Galewsky, J., Steen-Larsen, H. C., Field, R. D., Worden, J., Risi, C., & Schneider, M. (2016). Stable isotopes in atmospheric water vapor and applications to the hydrologic cycle. *Reviews of Geophysics*, *54*(4), 809–865. https://doi.org/10.1002/2015rg000512

Gao, L., Edwards, E. J., Zeng, Y., & Huang, Y. (2014). Major evolutionary trends in hydrogen isotope fractionation of vascular plant leaf waxes. *PLoS One*, *9*(11), e112610. https://doi.org/10.1371/journal.pone.0112610

Garcin, Y., Schefuß, E., Schwab, V. F., Garreta, V., Gleixner, G., Vincens, A., et al. (2014). Reconstructing C3 and C4 vegetation cover using n-alkane carbon isotope ratios in recent lake sediments from Cameroon, western central Africa. *Geochimica et Cosmochimica Acta*, *142*, 482–500. https://doi.org/10.1016/j.gca.2014.07.004

Ghil, M., Allen, M., Dettinger, M., Ide, K., Kondrashov, D., Mann, M., et al. (2002). Advanced spectral methods for climatic time series. *Reviews of Geophysics*, *40*(1), 3–1. https://doi.org/10.1029/2000rg000092

Ghil, M., & Vautard, R. (1991). Interdecadal oscillations and the warming trend in global temperature time series. *Nature*, *350*(6316), 324–327. https://doi.org/10.1038/350324a0

Hopmans, E. C., Schouten, S., & Damsté, J. S. S. (2016). The effect of improved chromatography on GDGT-based palaeoproxies. *Organic Geochemistry*, *93*, 1–6. https://doi.org/10.1016/j.orggeochem.2015.12.006

Hopmans, E. C., Weijers, J. W., Schefuß, E., Herfort, L., Damsté, J. S. S., & Schouten, S. (2004). A novel proxy for terrestrial organic matter in sediments based on branched and isoprenoid tetraether lipids. *Earth and Planetary Science Letters*, *224*(1–2), 107–116. https://doi.org/10.1016/j.epsl.2004.05.012

Howell, P., Pisias, N., Ballance, J., Baughman, J., & Ochs, L. (2006). *Arand time-series analysis software*. Brown University.

Jalihal, C., Bosmans, J. H. C., Srinivasan, J., & Chakraborty, A. (2019). The response of tropical precipitation to Earth's precession: The role of energy fluxes and vertical stability. *Climate of the Past*, *15*(2), 449–462. https://doi.org/10.5194/cp-15-449-2019

Kanamitsu, M., Ebisuzaki, W., Woollen, J., Yang, S.-K., Hnilo, J., Fiorino, M., & Potter, G. (2002). NCEP–DOE AMIP-II reanalysis (r-2). *Bulletin of the American Meteorological Society*, *83*(11), 1631–1644. https://doi.org/10.1175/bams-83-11-1631(2002)083<1631:nar>2.3.co;2

Kuechler, R., Schefuß, E., Beckmann, B., Dupont, L., & Wefer, G. (2013). NW African hydrology and vegetation during the last glacial cycle reflected in plant-wax-specific hydrogen and carbon isotopes. *Quaternary Science Reviews*, *82*, 56–67. https://doi.org/10.1016/j.quascirev.2013.10.013

Kusch, S., Rethemeyer, J., Schefuß, E., & Mollenhauer, G. (2010). Controls on the age of vascular plant biomarkers in Black Sea sediments. *Geochimica et Cosmochimica Acta*, *74*(24), 7031–7047. https://doi.org/10.1016/j.gca.2010.09.005

Laskar, J., Robutel, P., Joutel, F., Gastineau, M., Correia, A., & Levrard, B. (2004). A long-term numerical solution for the insolation quantities of the Earth. *Astronomy & Astrophysics*, *428*(1), 261–285. https://doi.org/10.1051/0004-6361:20041335

Lea, D. W. (2004). The 100,000-yr cycle in tropical SST, greenhouse forcing, and climate sensitivity. *Journal of Climate*, *17*(11), 2170–2179. https://doi.org/10.1175/1520-0442(2004)017<2170:tycits>2.0.co;2

LeGrande, A., & Schmidt, G. (2009). Sources of Holocene variability of oxygen isotopes in paleoclimate archives. *Climate of the Past*, *5*(3), 441–455. https://doi.org/10.5194/cp-5-441-2009

Lisiecki, L. E., & Raymo, M. E. (2005). A Pliocene-Pleistocene stack of 57 globally distributed benthic $\delta$18O records. *Paleoceanography*, *20*(1), PA1003. https://doi.org/10.1029/2004pa001071

Liu, Z., Wen, X., Brady, E., Otto-Bliesner, B., Yu, G., Lu, H., et al. (2014). Chinese cave records and the East Asia summer monsoon. *Quaternary Science Reviews*, *83*, 115–128. https://doi.org/10.1016/j.quascirev.2013.10.021

Locarnini, M., Mishonov, A., Baranova, O., Boyer, T., Zweng, M., Garcia, H., et al. (2018). World Ocean Atlas 2018, volume 1: Temperature.

Loeb, N. G., Doelling, D. R., Wang, H., Su, W., Nguyen, C., Corbett, J. G., et al. (2018). Clouds and the Earth's radiant energy system (CERES) energy balanced and filled (EBAF) top-of-atmosphere (TOA) edition-4.0 data product. *Journal of Climate*, *31*(2), 895–918. https://doi.org/10.1175/jcli-d-17-0208.1

Long, A., & Rippeteau, B. (1974). Testing contemporaneity and averaging radiocarbon dates. *American Antiquity*, *39*(2), 205–215. https://doi.org/10.2307/279583

Lopes dos Santos, R. A., Prange, M., Castañeda, I. S., Schefuß, E., Mulitza, S., Schulz, M., et al. (2010). Glacial–interglacial variability in Atlantic meridional overturning circulation and thermocline adjustments in the tropical north Atlantic. *Earth and Planetary Science Letters*, *300*(3–4), 407–414. https://doi.org/10.1016/j.epsl.2010.10.030

Lückge, A., Mohtadi, M., Rühlemann, C., Scheeder, G., Vink, A., Reinhardt, L., & Wiedicke, M. (2009). Monsoon versus ocean circulation controls on paleoenvironmental conditions off southern Sumatra during the past 300,000 years. *Paleoceanography*, *24*(1), PA1208. https://doi.org/10.1029/2008pa001627

McGrath, S. M., Clemens, S. C., Huang, Y., & Yamamoto, M. (2021). Greenhouse gas and ice volume drive Pleistocene Indian summer monsoon precipitation isotope variability. *Geophysical Research Letters*, *48*(4), e2020GL092249. https://doi.org/10.1029/2020gl092249

Merlis, T. M., Schneider, T., Bordoni, S., & Eisenman, I. (2013). The tropical precipitation response to orbital precession. *Journal of Climate*, *26*(6), 2010–2021. https://doi.org/10.1175/jcli-d-12-00186.1

Molnar, P., Boos, W. R., & Battisti, D. S. (2010). Orographic controls on climate and paleoclimate of Asia: Thermal and mechanical roles for the Tibetan Plateau. *Annual Review of Earth and Planetary Sciences*, *38*(1), 77–102. https://doi.org/10.1146/annurev-earth-040809-152456

Moore, M., Kuang, Z., & Blossey, P. (2014). A moisture budget perspective of the amount effect. *Geophysical Research Letters*, *41*(4), 1329–1335. https://doi.org/10.1002/2013gl058302

O'Mara, N. A., Skonieczny, C., McGee, D., Winckler, G., Bory, A. J.-M., Bradtmiller, L. I., et al. (2022). Pleistocene drivers of northwest African hydroclimate and vegetation. *Nature Communications*, *13*(1), 1–11. https://doi.org/10.1038/s41467-022-31120-x

Prahl, F. G., & Wakeham, S. G. (1987). Calibration of unsaturation patterns in long-chain ketone compositions for palaeotemperature assessment. *Nature*, *330*(6146), 367–369. https://doi.org/10.1038/330367a0

Rattanasriampaipong, R., Zhang, Y. G., Pearson, A., Hedlund, B. P., & Zhang, S. (2022). Archaeal lipids trace ecology and evolution of marine ammonia-oxidizing archaea. *Proceedings of the National Academy of Sciences of the United States of America*, *119*(31), e2123193119. https://doi.org/10.1073/pnas.2123193119

Roxy, M. K., Ritika, K., Terray, P., & Masson, S. (2014). The curious case of Indian Ocean warming. *Journal of Climate*, *27*(22), 8501–8509. https://doi.org/10.1175/jcli-d-14-00471.1

Ruddiman, W. F. (2006). Orbital changes and climate. *Quaternary Science Reviews*, *25*(23–24), 3092–3112. https://doi.org/10.1016/j.quascirev.2006.09.001

Sachse, D., Billault, I., Bowen, G. J., Chikaraishi, Y., Dawson, T. E., Feakins, S. J., et al. (2012). Molecular paleohydrology: Interpreting the hydrogen-isotopic composition of lipid biomarkers from photosynthesizing organisms. *Annual Review of Earth and Planetary Sciences*, *40*(1), 221–249. https://doi.org/10.1146/annurev-earth-042711-105535

Saji, N., Goswami, B., Vinayachandran, P., & Yamagata, T. (1999). A dipole mode in the tropical Indian Ocean. *Nature*, *401*(6751), 360–363. https://doi.org/10.1038/43854

Schefuß, E., Schouten, S., Jansen, J. F., & Damsté, J. S. S. (2003). African vegetation controlled by tropical sea surface temperatures in the mid-Pleistocene period. *Nature*, *422*(6930), 418–421. https://doi.org/10.1038/nature01500

Schneider, U., Becker, A., Finger, P., Meyer-Christoffer, A., Rudolf, B., & Ziese, M. (2011). GPCC full data reanalysis version 6.0 at 1.0°: Monthly land-surface precipitation from rain-gauges built on GTS-based and historic data.

Schneider, U., Ziese, M., Meyer-Christoffer, A., Finger, P., Rustemeier, E., & Becker, A. (2016). The new portfolio of global precipitation data products of the global precipitation climatology centre suitable to assess and quantify the global water cycle and resources. *Proceedings of the International Association of Hydrological Sciences*, *374*, 29–34. https://doi.org/10.5194/piahs-374-29-2016

Schott, F. A., & McCreary, J. P., Jr. (2001). The monsoon circulation of the Indian Ocean. *Progress in Oceanography*, *51*(1), 1–123. https://doi.org/10.1016/s0079-6611(01)00083-0

Schott, F. A., Xie, S.-P., & McCreary, J. P., Jr. (2009). Indian Ocean circulation and climate variability. *Reviews of Geophysics*, *47*(1), RG1002. https://doi.org/10.1029/2007rg000245

Schouten, S., Forster, A., Panoto, F. E., & Damsté, J. S. S. (2007). Towards calibration of the $TEX_{86}$ palaeothermometer for tropical sea surface temperatures in ancient greenhouse worlds. *Organic Geochemistry*, *38*(9), 1537–1546. https://doi.org/10.1016/j.orggeochem.2007.05.014

Schouten, S., Hopmans, E. C., Schefuß, E., & Damste, J. S. S. (2002). Distributional variations in marine crenarchaeotal membrane lipids: A new tool for reconstructing ancient sea water temperatures? *Earth and Planetary Science Letters*, *204*(1–2), 265–274. https://doi.org/10.1016/s0012-821x(02)00979-2

Skonieczny, C., McGee, D., Winckler, G., Bory, A., Bradtmiller, L., Kinsley, C. W., et al. (2019). Monsoon-driven Saharan dust variability over the past 240,000 years. *Science Advances*, *5*(1), eaav1887. https://doi.org/10.1126/sciadv.aav1887

Smith, F. A., & Freeman, K. H. (2006). Influence of physiology and climate on $\delta$D of leaf wax *n*-alkanes from $C_3$ and $C_4$ grasses. *Geochimica et Cosmochimica Acta*, *70*(5), 1172–1187. https://doi.org/10.1016/j.gca.2005.11.006

Tierney, J. E., & DeMenocal, P. B. (2013). Abrupt shifts in horn of Africa hydroclimate since the Last Glacial Maximum. *Science*, *342*(6160), 843–846. https://doi.org/10.1126/science.1240411

Tierney, J. E., deMenocal, P. B., & Zander, P. D. (2017a). A climatic context for the out-of-Africa migration. *Geology*, *45*(11), 1023–1026. https://doi.org/10.1130/g39457.1

Tierney, J. E., deMenocal, P. B., & Zander, P. D. (2017b). NOAA/WDS paleoclimatology—Gulf of Aden 200,000 year stable isotope and alkenone SST data [Dataset]. National Oceanic and Atmospheric Administration. https://doi.org/10.25921/k92a-8583

Tierney, J. E., Lewis, S. C., Cook, B. I., LeGrande, A. N., & Schmidt, G. A. (2011). Model, proxy and isotopic perspectives on the east African humid period. *Earth and Planetary Science Letters*, *307*(1–2), 103–112. https://doi.org/10.1016/j.epsl.2011.04.038

Tierney, J. E., Pausata, F. S., & deMenocal, P. B. (2017). Rainfall regimes of the green Sahara. *Science Advances*, *3*(1), e1601503. https://doi.org/10.1126/sciadv.1601503

Tierney, J. E., Smerdon, J. E., Anchukaitis, K. J., & Seager, R. (2013). Multidecadal variability in east African hydroclimate controlled by the Indian Ocean. *Nature*, *493*(7432), 389–392. https://doi.org/10.1038/nature11785

Tierney, J. E., & Tingley, M. P. (2015). A $TEX_{86}$ surface sediment database and extended Bayesian calibration. *Scientific Data*, *2*(1), 1–10. https://doi.org/10.1038/sdata.2015.29

Tierney, J. E., & Tingley, M. P. (2018). BAYSPLINE: A new calibration for the alkenone paleothermometer. *Paleoceanography and Paleoclimatology*, *33*(3), 281–301. https://doi.org/10.1002/2017pa003201

Tokinaga, H., Xie, S.-P., Timmermann, A., McGregor, S., Ogata, T., Kubota, H., & Okumura, Y. M. (2012). Regional patterns of tropical Indo-Pacific climate change: Evidence of the Walker Circulation weakening. *Journal of Climate*, *25*(5), 1689–1710. https://doi.org/10.1175/jcli-d-11-00263.1

Vautard, R., Yiou, P., & Ghil, M. (1992). Singular-spectrum analysis: A toolkit for short, noisy chaotic signals. *Physica D: Nonlinear Phenomena*, *58*(1–4), 95–126. https://doi.org/10.1016/0167-2789(92)90103-t

Volkman, J., Johns, R., Gillan, F., Perry, G., & Bavor, H., Jr. (1980). Microbial lipids of an intertidal sediment—I. Fatty acids and hydrocarbons. *Geochimica et Cosmochimica Acta*, *44*(8), 1133–1143. https://doi.org/10.1016/0016-7037(80)90067-8

Waelbroeck, C., Labeyrie, L., Michel, E., Duplessy, J. C., McManus, J., Lambeck, K., et al. (2002). Sea-level and deep water temperature changes derived from benthic foraminifera isotopic records. *Quaternary Science Reviews*, *21*(1–3), 295–305. https://doi.org/10.1016/s0277-3791(01)00101-9

Wang, Y.-J., Cheng, H., Edwards, R. L., An, Z., Wu, J., Shen, C.-C., & Dorale, J. A. (2001). A high-resolution absolute-dated late Pleistocene monsoon record from Hulu Cave, China. *Science*, *294*(5550), 2345–2348. https://doi.org/10.1126/science.1064618

Windler, G., Tierney, J. E., & Anchukaitis, K. J. (2021). Glacial-interglacial shifts dominate tropical indo-Pacific hydroclimate during the late pleistocene. *Geophysical Research Letters*, *48*(15), e2021GL093339. https://doi.org/10.1029/2021gl093339

Windler, G., Tierney, J. E., & deMenocal, P. B. (2022). NOAA/WDS paleoclimatology—VM19-193, Indian Ocean, 250,000 year long biomarker reconstructions [Dataset]. National Oceanic and Atmospheric Administration. https://doi.org/10.25921/bx6z-sd71

Windler, G., Tierney, J. E., DiNezio, P. N., Gibson, K., & Thunell, R. (2019a). NOAA/WDS paleoclimatology—Indo-Pacific Warm Pool 450,000 year alkenone temperature reconstructions [Dataset]. National Oceanic and Atmospheric Administration. https://doi.org/10.25921/7dtq-9x28

Windler, G., Tierney, J. E., DiNezio, P. N., Gibson, K., & Thunell, R. (2019b). Shelf exposure influence on Indo-Pacific Warm Pool climate for the last 450,000 years. *Earth and Planetary Science Letters*, *516*, 66–76. https://doi.org/10.1016/j.epsl.2019.03.038

Windler, G., Tierney, J. E., Zhu, J., & Poulsen, C. J. (2020). Unravelling glacial hydroclimate in the Indo-Pacific Warm Pool: Perspectives from water isotopes. *Paleoceanography and Paleoclimatology*, e2020PA003985. https://doi.org/10.1029/2020PA003985

Wuchter, C., Schouten, S., Coolen, M. J., & Sinninghe Damsté, J. S. (2004). Temperature-dependent variation in the distribution of tetraether membrane lipids of marine crenarchaeota: Implications for tex86 paleothermometry. *Paleoceanography*, *19*(4), PA4028. https://doi.org/10.1029/2004pa001041

Zhang, Y. G., Pagani, M., & Wang, Z. (2016). Ring index: A new strategy to evaluate the integrity of $TEX_{86}$ paleothermometry. *Paleoceanography*, *31*(2), 220–232. https://doi.org/10.1002/2015pa002848

Zhang, Y. G., Zhang, C. L., Liu, X.-L., Li, L., Hinrichs, K.-U., & Noakes, J. E. (2011). Methane index: A tetraether archaeal lipid biomarker indicator for detecting the instability of marine gas hydrates. *Earth and Planetary Science Letters*, *307*(3–4), 525–534. https://doi.org/10.1016/j.epsl.2011.05.031